

MPM Simulation of Dynamic Material Failure with a Decohesion Constitutive Model

D. Sulsky

Department of Mathematics and Statistics
University of New Mexico
Albuquerque, NM 87131
sulsky@math.unm.edu

H. L. Schreyer

Department of Mechanical Engineering
University of New Mexico
Albuquerque, NM 87131
schreyer@me.unm.edu

July, 2003

Send proofs to:

D. Sulsky
Department of Mathematics and Statistics
University of New Mexico
Albuquerque, NM 87131

FAX: 505-277-5505

EMAIL: sulsky@math.unm.edu

Keywords: Decohesion, Discrete Constitutive Model, Dynamic Failure, Material-Point Method, Sinusoidal Pulse, Spall.

Abstract

An initiation criterion is developed for a discrete constitutive equation model of material failure. The decohesion constitutive model is combined with elasticity and implemented in the numerical material-point method. The complete numerical procedure is used to study spall failure in brittle materials. A one-dimensional analytical solution for a bar subjected to a sinusoidal pulse is derived and used to verify the numerical method. The sinusoidal pulse leads to a finite region of the bar undergoing failure, rather than a single plane, as occurs with a square or triangular wave pulse. This observation may be related to experimental findings of multiple spall planes for impacted bars. The numerical method is not restricted to one-dimensional problems, thus we further study the additional features that arise for an impacted bar assuming that the bar deforms under plane stress conditions. Reflections of stress waves from the lateral surfaces of the bar result in the appearance of curved and secondary spall surfaces.

1 Introduction

Modeling material failure is still a theoretically and numerically challenging problem. Numerical simulation of dynamic, brittle fracture has been carried out using continuum damage models (Seaman *et al.*, 1985; Curran, *et al.*, 1987; Walter, 1992; Johnson, *et al.*, 1992; Rajendran, 1994), and more recently using cohesive theories (Miehe and Schröder, 1994; Camacho and Ortiz, 1996; Ortiz and Pandolfi, 1999; Pandolfi *et al.*, 2000; Schreyer, *et al.*, 2002; Armero, 2002). The cohesive theories provide a discrete approach where material failure is treated as a strong discontinuity in displacement with traction related to the discontinuity. There is a rich history in which discrete constitutive equations are postulated directly as reflected by Barenblatt (1959), Hillerborg *et al.* (1976), Needleman (1987), and Planas *et al.* (1995). Feenstra *et al.* (1991a,b), and Corigliano (1993) provide a nice summary of previous models and describe numerical methods based on interface elements. The use of constraint elements is a related approach (Reedy *et al.*, 1997). The work of Ortiz and coworkers (Camacho and Ortiz, 1996; Ortiz and Pandolfi, 1999; Pandolfi *et al.*, 2000) uses special cohesive elements to implement their constitutive model to obtain a robust formulation with correct propagation speeds and energy release. Dvorkin *et al.* (1990) describe an alternative approach whereby discontinuities are handled at the element level rather than enforcing discontinuities along element boundaries. Wells and Sluys (2000a,b) have extended the concept with impressive results. A different approach for arriving at a description of failure is provided by Simo *et al.* (1993) in which the continuum constitutive equation is extended beyond the loss of ellipticity condition into the softening regime. They introduce distribution theory in the softening regime, which leads to a strong discontinuity. The theory has since been extensively developed by Oliver and Simo (1994); Armero and Garikipati (1996); Larsson and Runesson (1996); Oliver (1996a,b, 2000); and Armero (1999). The final result is also a discrete constitutive equation relating stress to the discontinuity in displacement, and here also the discontinuity is handled at the element or constitutive level.

Miehe and Schröder (1994); and Schreyer, *et al.* (2002) introduce a decohesion constitutive model which falls in the category of a discrete constitutive equation that is invoked when the effective traction on the decohesion surface reaches a critical value. The effective traction criterion allows arbitrary failure modes, and is expressed in terms of measurable material properties. The model relates the effective traction to the jump in displacement, resulting in a strong discontinuity. The decohesion constitutive model is invoked to model the failure process, but the material behavior prior to failure can be modeled independently. Thus, brittle and ductile materials can be treated with different constitutive descriptions prior to the initiation of failure and the decohesion model can include varying amounts of dissipation based on the material ductility. Schreyer, *et al.* (2002) assume the normal to the decohesion surface is known, *a priori*. Here, we determine the normal to the surface by finding the direction in which the effective traction is largest. Section 2 reviews the constitutive model and presents the method for determining the direction of the failure surface.

There have been extensive experimental studies of spall failure in brittle materials, see Grady and Kipp (1979), for one example. Spall failure can also be studied analytically

by propagating an initially compressive wave down a bar until it encounters a free end, whereupon the reflected pulse becomes tensile. Square and triangular wave pulses result in a clean spall plane (Zukas, 1982; Armero, 2002). However, experimentally applied impulses can have a smoother profile (Clos, *et al.*, 1991; Brara, *et al.*, 2001). Section 3 examines spall due to a sinusoidal pulse travelling down a bar, assuming either uniaxial stress or strain. An analytical solution is presented for the initial stages of decohesion up to the point where separation occurs in the bar and two pieces are formed. Surprisingly, spall patterns are more complicated for the sinusoidal pulse as compared to square or triangular waves; in particular failure does not occur at a single point, but is distributed over a segment of the bar. This feature might be related to empirical evidence of multiple spall planes (Shockey, *et al.*, 1974; Brara, *et al.*; 2001).

The decohesive constitutive model is implemented in the material-point method (MPM) (Sulsky, *et al.*, 1994, 1995, 1996). Section 4 presents a short summary of the MPM and the implementation of the decohesion model therein. In Section 5, the analytical solution for the dynamic failure of the one-dimensional bar problem under uniaxial strain is used to verify the numerical procedure. Also in this section, the same problem is solved assuming plane stress. The more complicated wave structure leads to a likewise more complicated failure pattern. The numerical simulations show the flexibility of the discrete decohesion constitutive equation in combination with MPM as a model for dynamic failure.

2 Decohesion Constitutive Equation

Schreyer, *et al.* (2002) developed a class of discrete constitutive equations using a general thermodynamic framework which insures that the dissipation inequality (2nd law) is automatically satisfied. Each model in the class is determined by choosing (i) an expression for the free energy, (ii) the failure function that describes when decohesion takes place, and (iii) the evolution equations for the opening displacement. This derivation and formulation of the discrete constitutive equation is analogous to what one might use for a rigid-plastic continuum where the elastic part of the response is ignored, *i.e.*, the total strain and the plastic strain are identical. Then the elastic internal strain energy does not exist and the stress must be provided by the solution to a boundary value problem. We summarize the derivation of the constitutive model and present one choice for the free energy, failure function and associated evolution equations used in the subsequent two-dimensional numerical simulations.

A reasonable assumption for brittle materials is that the stress is purely elastic in the undamaged material. For now, it is assumed that failure is initiated on a surface with normal, \mathbf{n} , given. The initiation of a new failure surface is addressed below. In the two-dimensional simulations, the failure surface is assumed to be orthogonal to the simulation plane. Thus, the failure surface intersects the simulation plane along a curve. Given the stress, $\boldsymbol{\sigma}$, and the unit normal, \mathbf{n} , of a potential failure surface, the traction on the surface is $\boldsymbol{\tau} = \boldsymbol{\sigma} \cdot \mathbf{n}$. The normal component of the traction is $\tau_n = \boldsymbol{\tau} \cdot \mathbf{n}$, and tangential component $\tau_t = \boldsymbol{\tau} \cdot \mathbf{t}$, where \mathbf{t} is tangent to the failure surface in the two-dimensional plane.

We assume that the surface energy per unit area, U , depends on a dimensionless, scalar parameter, u^{eff} , that provides a measure of the amount of decohesion. This parameter is chosen to be monotonically increasing, so that $u^{\text{eff}} = 0$ denotes no decohesion and $u^{\text{eff}} = 1$ indicates that decohesion is complete and the material has separated into two pieces. Using the parameter u^{eff} , the evolution equation for the discontinuity in displacement at the surface of material failure is taken to be

$$\dot{\mathbf{u}}^d = \dot{u}^{\text{eff}} \mathbf{m}, \quad (1)$$

where \mathbf{m} is the failure mode, and \mathbf{u}^d is the opening displacement. Note that \mathbf{m} has the dimensions of length, consistent with an opening displacement. The opening displacement represents the permanent jump in displacement at the failure surface due to the decohesion process.

The dissipation power is defined as

$$\dot{D} = \boldsymbol{\tau} \cdot \dot{\mathbf{u}}^d - \dot{U}. \quad (2)$$

If a parameter $\bar{\tau}$ conjugate to u^{eff} is defined as

$$\bar{\tau} = -\frac{\partial U}{\partial u^{\text{eff}}}, \quad (3)$$

then the dissipation power becomes

$$\dot{D} = (\hat{\tau}^{\text{eff}} + \bar{\tau}) \dot{u}^{\text{eff}}, \quad (4)$$

where $\hat{\tau}^{\text{eff}} = \boldsymbol{\tau} \cdot \mathbf{m}$.

A failure function, $F(\bar{\tau}, \boldsymbol{\tau})$ is typically chosen so that (i) $F(0, \mathbf{0}) < 0$, (ii) evolution of damage occurs only if $F = 0$, (iii) $F > 0$ is not allowed, and (iv) $\dot{D} \geq 0$. A particular model is obtained by choosing specific forms for U , F and \mathbf{m} . Alternatively, we can choose U , F , $\hat{\tau}^{\text{eff}}$, and then enforce an associated evolution rule, $\mathbf{m} = \partial F / \partial \boldsymbol{\tau}$. We adopt the latter approach for the following elementary model. First, select

$$U = U_0 \left(1 - \frac{1}{2} (u^{\text{eff}})^2 \right) \quad U_0 > 0. \quad (5)$$

This choice implies there is an initial surface energy, U_0 , that is reduced when decohesion occurs. Note that,

$$\bar{\tau} = -\frac{\partial U}{\partial u^{\text{eff}}} = U_0 u^{\text{eff}}. \quad (6)$$

Next, we choose

$$F = \hat{\tau}^{\text{eff}} + \bar{\tau} - U_0. \quad (7)$$

When $F = 0$, $\hat{\tau}^{\text{eff}} + \bar{\tau} = U_0$, so the dissipation power becomes $\dot{D} = U_0 \dot{u}^{\text{eff}} \geq 0$, and the second law of thermodynamics is satisfied.

Finally, we adopt

$$\hat{\tau}^{\text{eff}} = U_0 \left(\left(\frac{\tau_n}{\tau_{nf}} \right)^2 + \left(\frac{\tau_t}{\tau_{tf}} \right)^2 \right)^{1/2}. \quad (8)$$

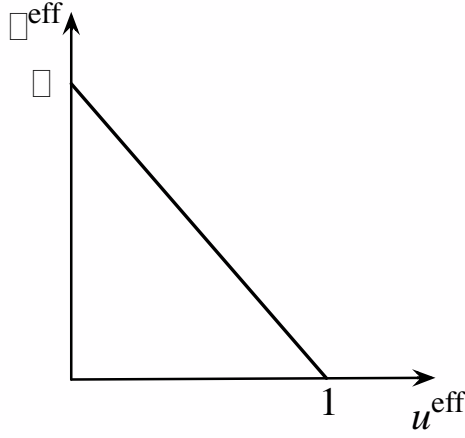


Figure 1: The decohesion relation is a linear decay in the effective traction as a function of the effective opening displacement on the failure surface. The fracture energy is the area under the curve.

The expression for the effective traction contains two material parameters, τ_{nf} and τ_{tf} , that are discussed below. The resulting associated evolution for the decohesion is

$$\mathbf{m} = \frac{U_0^2}{\hat{\tau}^{\text{eff}}} \left(\frac{\tau_n}{\tau_{nf}^2} \mathbf{n} + \frac{\tau_t}{\tau_{tf}^2} \mathbf{t} \right). \quad (9)$$

Substituting (6) into (7), we obtain

$$F = \hat{\tau}^{\text{eff}} - U_0(1 - u^{\text{eff}}). \quad (10)$$

When decohesion occurs, $F = 0$, and the dimensionless parameter $\tau^{\text{eff}} = \hat{\tau}^{\text{eff}}/U_0$ is linearly related to u^{eff} . Figure 1 depicts this simple linear relationship between the dimensionless effective traction on the failure surface and the dimensionless effective opening displacement.

There are three material parameters associated with this model, τ_{nf} , τ_{tf} and U_0 . Suppose $\tau_t = 0$ and there is no decohesion, $u^{\text{eff}} = 0$. Decohesion is initiated when $F = 0$. Using (8) in (10), decohesion is initiated when $\tau_n = \tau_{nf}$. Thus, the material parameter τ_{nf} is the failure traction for a pure opening mode. Similarly, τ_{tf} is the failure traction in pure shear. Since $\dot{D} = U_0 \dot{u}^{\text{eff}}$, we have $D = U_0 u^{\text{eff}}$. At separation $u^{\text{eff}} = 1$, and the total energy dissipated per unit surface area due to decohesion is U_0 . We also note, from the definition of U , (5), that the stored surface energy per unit area lost due to decohesion is $-U_0(u^{\text{eff}})^2/2$. At separation, the total energy per unit area lost is $-U_0/2$. The fracture energy is the energy per unit area that must be provided to cause separation, and it is the sum of the stored and dissipated energy. Thus, the fracture energy is $U_0/2$.

Failure Initiation

For each material point, at each loading step, $\tau^{\text{eff}} = \hat{\tau}^{\text{eff}}/U_0$, (Eq. 8), must be evaluated to determine if decohesion occurs. The failure surface is chosen by monitoring τ^{eff} , parameterized by normal vectors to a potential surface, and choosing the direction \mathbf{n} that first causes τ^{eff} to exceed one (or causes it to exceed one by the largest amount). This criterion initiates failure on a surface with normal \mathbf{n} and thereafter the failure direction remains fixed for the material point as possible additional decohesion occurs.

In other words, to implement the initiation criterion one has to find the maximum value of τ^{eff} as a function of \mathbf{n} . Equivalently, the maximum of

$$(\tau^{\text{eff}}\tau_{nf})^2 = \tau_n^2 + \beta^2\tau_t^2 \quad \text{where} \quad \beta^2 = (\tau_{nf}/\tau_{tf})^2 \quad (11)$$

can be used. Let $\boldsymbol{\sigma}$ be the current stress. The principal stresses are denoted σ_1 and σ_2 , and unit vectors are given by $(\cos\theta, \sin\theta)$ for $\theta \in [0, \pi]$ in principal coordinates. Then, in principal coordinates, Eq. 11 becomes

$$f(\theta) \equiv (\tau^{\text{eff}}\tau_{nf})^2 = \frac{1}{4}(\sigma_1 + \sigma_2)^2 + \frac{1}{4}\beta^2(\sigma_2 - \sigma_1)^2 + \frac{1}{2}(\sigma_1^2 - \sigma_2^2)\cos 2\theta + \frac{1}{4}(\sigma_2 - \sigma_1)^2(1 - \beta^2)\cos^2 2\theta. \quad (12)$$

The maximum of Eq. 12, as a function of θ , occurs when $f'(\theta) = 0$, or when (i) $\sin 2\theta = 0$, (ii) $\cos 2\theta = (\sigma_1 + \sigma_2)/(\sigma_2 - \sigma_1)(1 - \beta^2)$ (if the right-hand side is less than or equal to one in magnitude), or (iii) $\sigma_1 = \sigma_2$ (then $f(\theta) = \sigma$, a constant).

Case(i): $\sin 2\theta = 0$ ($\theta = 0$ or $\pi/2$). In this case, failure occurs with the normal in the direction of maximum principal stress and

$$(\tau^{\text{eff}}\tau_{nf})^2 = \sigma_1^2 \quad \text{or} \quad \sigma_2^2, \quad (13)$$

whichever is larger.

Case(ii): $\cos 2\theta = (\sigma_1 + \sigma_2)/(\sigma_2 - \sigma_1)(1 - \beta^2)$. If the right-hand side of this equation is less than or equal to one in magnitude, there is a possible failure surface with a normal whose components are

$$\begin{aligned} \cos(\theta) &= \pm \frac{1}{\sqrt{2}} \left[1 + \frac{\sigma_1 + \sigma_2}{\sigma_2 - \sigma_1} \frac{1}{1 - \beta^2} \right]^{1/2} \\ \sin(\theta) &= \pm \frac{1}{\sqrt{2}} \left[1 - \frac{\sigma_1 + \sigma_2}{\sigma_2 - \sigma_1} \frac{1}{1 - \beta^2} \right]^{1/2} \end{aligned}$$

and

$$(\tau^{\text{eff}}\tau_{nf})^2 = \frac{1}{4}\beta^2 \left[(\sigma_1 - \sigma_2)^2 - \frac{(\sigma_1 + \sigma_2)^2}{1 - \beta^2} \right]. \quad (14)$$

Case(iii): $\sigma_1 = \sigma_2$. This is a degenerate case of hydrostatic pressure where failure is equally likely in any direction. An arbitrary direction is chosen.

Algorithmically, at each loading step, we compute Eq. 13 and Eq. 14. If τ^{eff} exceeds one for one of these values then failure is initiated with a failure surface given by the corresponding \mathbf{n} . The normal to the failure surface remains fixed for future loading/unloading of the material point.

We remark that if $\beta \rightarrow 0$, mode I failure is expected since the shear failure strength is much greater than the tensile failure strength, $\tau_{tf} \gg \tau_{nf}$. In the above analysis, case (ii) will never yield the maximum effective traction since $\beta = 0$ in Eq. 14. Therefore failure will occur with the normal in the direction of maximum principal stress. On the other hand, if $\beta \rightarrow \infty$,

$$\left| \frac{\sigma_1 + \sigma_2}{\sigma_2 - \sigma_1} \frac{1}{1 - \beta^2} \right| \leq 1$$

for β large enough (except when $\sigma_1 = \sigma_2$) and τ^{eff} given by Eq. 14 will correspond to the maximum value. The normal to the failure surface becomes $(\cos \theta, \sin \theta) = (\pm 1/\sqrt{2}, \pm 1/\sqrt{2})$ in this limit, and mode II failure occurs.

3 Spall due to a Sinusoidal Pulse

In this section, we analyze spall failure in a one-dimensional bar. A compressive, sinusoidal pulse is propagated down a bar until it interacts with a free end. The resultant reflected, tensile wave can cause material failure if the peak stress is large enough. Triangular (Zuckas, 1982) and rectangular (Armero, 2001; Camacho and Ortiz, 1996) wave pulses have been analyzed before. In these cases, there is a unique spall plane and a clean fracture. Surprisingly, a smooth wave pulse results in failure distributed over a region of the bar. Although convenient for analysis, triangular and rectangular pulses may not be representative of pulses observed experimentally. Inelastic deformation will smooth the leading part of a wave, and it is difficult to release an applied field abruptly. Therefore, smooth pulses might be more representative of pulses observed experimentally. A sinusoidal pulse is chosen to illustrate the features that might arise with smooth pulses.

Wave Solution with no Failure

Consider a bar of unit cross section. To limit the scope of the investigation, we restrict ourselves to uniaxial stress or uniaxial strain, and to continuum elasticity. Let E denote the elastic modulus and ρ_0 the density. For uniaxial stress, E is the Young's modulus, Y ; and for uniaxial strain, $E = Y(1 - \nu)/((1 + \nu)(1 - 2\nu))$, where ν is Poisson's ratio. Let u denote the displacement with strain and stress defined by $e = \partial u / \partial x$ and $\sigma = Ee$, respectively. The equation of motion is

$$c^2 \frac{\partial^2 u}{\partial x^2} = \ddot{u} \qquad c^2 = E/\rho_0 \qquad (15)$$

where a superposed dot denotes a partial derivative with respect to time, t , and c is the wave speed.

The material failure surface is assumed to be a plane with a normal vector aligned along the center line of the bar. Thus, failure is in the direction of the nonzero stress $\sigma > 0$ component, with $\tau_n = \sigma$ and $\tau_t = 0$. We use the notation, τ_m to denote the maximum stress that can be supported. The effective traction τ^{eff} reduces to $\tau^{\text{eff}} = \tau_n/\tau_{nf}$. Failure occurs when $\tau^{\text{eff}} = 1$ or when $\sigma = \tau_n = \tau_m = \tau_{nf}$. The failure mode in this problem is

$$\mathbf{m} = \frac{U_0}{\tau_{nf}} \mathbf{n}. \quad (16)$$

So, the opening displacement only has a normal component, $\mathbf{u}^d = [u]\mathbf{n}$. The evolution equation, (1), becomes

$$[\dot{u}] = \dot{u}^{\text{eff}} \frac{U_0}{\tau_{nf}} \quad \text{or} \quad [u] = u^{\text{eff}} \frac{U_0}{\tau_{nf}}. \quad (17)$$

If separation occurs physically when $[u]$ reaches the value u_s then $u_s = U_0/\tau_{nf}$, because $u^{\text{eff}} = 1$ at separation. Thus we have $u^{\text{eff}} = [u]/u_s$ and the failure criterion, $F = 0$, reduces to

$$\tau_n = \tau_m (1 - [u]/u_s) \quad 0 \leq [u] \leq u_s. \quad (18)$$

Failure is not initiated until the traction attains the maximum value, τ_m . Failure evolves as the displacement discontinuity increases from zero to the value, u_s , which is the discontinuity at separation. After separation, two new free surfaces exist.

Consider a semi-infinite bar $x \geq 0$, with $x = 0$ denoting a free surface. First we give the elastic wave solution to (15) for a sinusoidal pulse of duration, t_D , travelling to the left and reaching the end $x = 0$ at time $t = 0$. The displacement, u , velocity, v , and stress, σ , are

$$u_i(x, t) = -\frac{v_z}{2} \left\{ \left(t + \frac{x}{c} \right) - \frac{t_D}{2\pi} \sin \frac{2\pi}{t_D} \left(t + \frac{x}{c} \right) \right\} \left\{ H\left(t + \frac{x}{c}\right) - H\left(t + \frac{x}{c} - t_D\right) \right\} \\ - \frac{v_z}{2} t_D H\left(t + \frac{x}{c} - t_D\right) \quad (19)$$

$$v_i(x, t) = -\frac{v_z}{2} \left\{ 1 - \cos \frac{2\pi}{t_D} \left(t + \frac{x}{c} \right) \right\} \left\{ H\left(t + \frac{x}{c}\right) - H\left(t + \frac{x}{c} - t_D\right) \right\} \quad (20)$$

$$\sigma_i(x, t) = -\frac{\sigma_z}{2} \left\{ 1 - \cos \frac{2\pi}{t_D} \left(t + \frac{x}{c} \right) \right\} \left\{ H\left(t + \frac{x}{c}\right) - H\left(t + \frac{x}{c} - t_D\right) \right\} \quad (21)$$

in which the subscript i is used to indicate that this is the initial pulse. The Heaviside function is denoted by H . The magnitude of the stress pulse is σ_z . Associated with this stress is a reference velocity v_z defined as

$$v_z = \frac{\sigma_z}{\rho_0 c} = c \frac{\sigma_z}{E}. \quad (22)$$

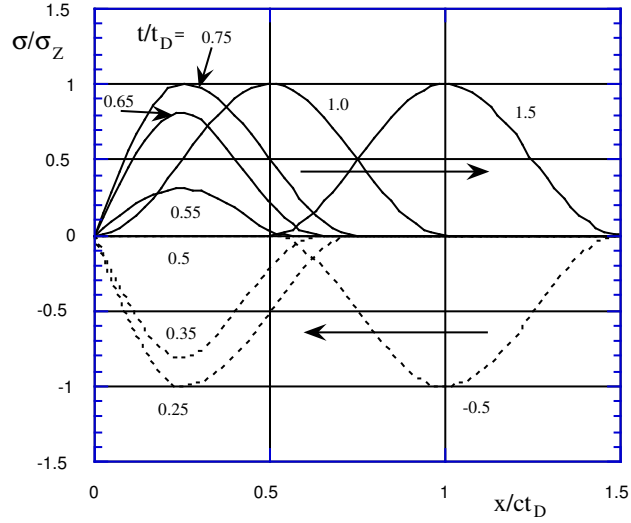


Figure 2: Stress as a function of dimensionless position x/ct_D for a sinusoidal wave impinging a free end, at various dimensionless times, t/t_D .

For $t > 0$, we must add the reflected wave (subscript r) which is described as follows:

$$u_r(x, t) = -\frac{v_z}{2} \left\{ \left(t - \frac{x}{c} \right) - \frac{t_D}{2\pi} \sin \frac{2\pi}{t_D} \left(t - \frac{x}{c} \right) \right\} \left\{ H\left(t - \frac{x}{c}\right) - H\left(t - \frac{x}{c} - t_D\right) \right\} - \frac{v_z}{2} t_D H\left(t - \frac{x}{c} - t_D\right) \quad (23)$$

$$v_r(x, t) = -\frac{v_z}{2} \left\{ 1 - \cos \frac{2\pi}{t_D} \left(t - \frac{x}{c} \right) \right\} \left\{ H\left(t - \frac{x}{c}\right) - H\left(t - \frac{x}{c} - t_D\right) \right\} \quad (24)$$

$$\sigma_r(x, t) = \frac{\sigma_z}{2} \left\{ 1 - \cos \frac{2\pi}{t_D} \left(t - \frac{x}{c} \right) \right\} \left\{ H\left(t - \frac{x}{c}\right) - H\left(t - \frac{x}{c} - t_D\right) \right\}. \quad (25)$$

If failure does not occur, the total stress is simply

$$\sigma = \sigma_i + \sigma_r. \quad (26)$$

A plot of the stress distribution for various times is shown in Fig. 2. For $t < t_D/2$, the stress is negative everywhere. When $t = t_D/2$, the stress is zero and for $t > t_D/2$, the stress is positive.

For $0.25 < t/t_D < 0.75$ and for $0 < x/ct_D < 0.25$, the Heaviside functions can be dropped and the stress is

$$\begin{aligned} \sigma &= -\frac{\sigma_z}{2} \left\{ 1 - \cos \frac{2\pi}{t_D} \left(t + \frac{x}{c} \right) \right\} + \frac{\sigma_z}{2} \left\{ 1 - \cos \frac{2\pi}{t_D} \left(t - \frac{x}{c} \right) \right\} \\ &= -\sigma_z \sin\left(\frac{2\pi t}{t_D}\right) \sin\left(\frac{2\pi x}{ct_D}\right). \end{aligned} \quad (27)$$

The point closest to the origin (the free surface) at which the minimum and maximum values of stress can be achieved is $x_F = ct_D/4$ for this time interval. When $t/t_D = 0.75$ the maximum stress of σ_z is attained. For $t/t_D > 0.75$, the maximum stress remains constant at σ_z but the location of maximum stress moves to the right. For $t > t_D$, the wave is a pure reflection of the original sinusoidal compressive wave.

Wave Solution Including Failure

Failure will not initiate if $\sigma_z < \tau_m$, but it will initiate at the point of maximum tensile stress ($x = x_F$) for $\sigma_z > \tau_m$ when the traction reaches the value τ_m . The time of failure initiation ($t = t_F$) is obtained from (27) by setting $\sigma = \tau_m$ and $x = x_F$, or

$$\tau_m = -\sigma_z \sin \frac{2\pi t_F}{t_D}. \quad (28)$$

The limiting cases of $\tau_m = 0$ and $\tau_m = \sigma_z$ yield $t_F = t_D/2$ and $t_F = 3t_D/4$, respectively.

It is convenient to introduce the parameter, φ_F , which denotes the time when fracture initiates as a fraction of the pulse duration after the first appearance of tensile stress

$$t_F = (0.5 + \varphi_F)t_D \quad (29)$$

with $0 < \varphi_F < 0.25$. Then (28) becomes

$$\tau_m/\sigma_z = \sin 2\pi\varphi_F. \quad (30)$$

The ratio τ_m/σ_z is a dimensionless parameter that, once specified, provides the failure initiation time, t_F . For example, if $\tau_m = 0.75\sigma_z$, then $\varphi_F = 0.135$ and $t_F = 0.635t_D$. In particular, note that $x_F \neq ct_F$.

Once failure is initiated, we postulate that waves are initiated traveling to the left and to the right of the failure point. For $t \geq t_F$,

$$\begin{aligned} u_{R,d}(x, t) &= v_z G(t - x/c - t_R) & u_{L,d}(x, t) &= -v_z G(t + x/c - t_L) \\ v_{R,d}(x, t) &= v_z G'(t - x/c - t_R) & v_{L,d}(x, t) &= -v_z G'(t + x/c - t_L) \\ \sigma_{R,d}(x, t) &= -\sigma_z G'(t - x/c - t_R) & \sigma_{L,d}(x, t) &= -\sigma_z G'(t + x/c - t_L) \end{aligned} \quad (31)$$

in which the shifted times are

$$t_R = t_F - \frac{x_F}{c} \quad t_L = t_F + \frac{x_F}{c}. \quad (32)$$

The subscripts R, d and L, d denote decohesive waves travelling to the right and left, respectively. The unknown function G is to be determined by satisfying the decohesive constitutive equation. A prime denotes a derivative with respect to the argument. The form of (31) provides stress continuity at $x = x_F$. The stress at the failure point consists of the sum of the initial and reflected waves and either $\sigma_{R,d}$ or $\sigma_{L,d}$

$$\sigma|_{x=x_F} = -\sigma_z \sin 2\pi t/t_D - \sigma_z G'|_{x=x_F}. \quad (33)$$

On the other hand, the difference of the displacement fields defined by the right and left propagating waves at $x = x_F$ provides a displacement discontinuity

$$[u]|_{x=x_F} = u_{R,d}|_{x=x_F} - u_{L,d}|_{x=x_F} = 2v_z G|_{x=x_F} \quad (34)$$

Substitute terms from (33) and (34), and note that $\tau_n = \sigma|_{x=x_F}$; thus, the decohesion constitutive equation of (18) at $x = x_F$ becomes

$$G'(t - t_F) - \frac{1}{t^*} G(t - t_F) = -\frac{\tau_m}{\sigma_z} - \sin 2\pi t/t_D \quad t_F \leq t \leq t_F + \Delta t_s \quad (35)$$

in which Δt_s is the time required to obtain separation once failure is initiated. The characteristic time t^* that arises from the equation is defined through material properties

$$t^* = \frac{u_s}{2v_z} \frac{\sigma_z}{\tau_m} = \frac{\rho_0 c u_s}{2\tau_m} = \frac{\rho_0 c}{2S} \quad S = \tau_m/u_s. \quad (36)$$

Note that if failure is not completed by the time $t = 3t_D/4$, then a different solution exists because the expression for the stress, (27), is no longer valid. We impose the initial decohesion condition that the displacement discontinuity is zero when $t = t_F$, or $G(0) = 0$. It follows from (28) and (35) that $G'(0) = 0$. Hence, from (28) and (33), the starting value for the stress is τ_m when decohesion is initiated.

The governing equation for decohesion (35) contains the characteristic time of material failure, t^* , and the duration of the forcing pulse, t_D . These characteristic times might very well be of different orders of magnitude. To conveniently capture the ratio of these two time scales, we define the following dimensionless parameter

$$r_D^* = 2\pi t^*/t_D \quad (37)$$

In addition, we convert to a shifted time

$$\hat{t} = t - t_F. \quad (38)$$

The right-most term of (35) becomes

$$\begin{aligned} \sin 2\pi t/t_D &= \sin 2\pi t_F/t_D \cos r_D^* \hat{t}/t^* + \cos 2\pi t_F/t_D \sin r_D^* \hat{t}/t^* \\ &= -\sin 2\pi \varphi_F \cos r_D^* \hat{t}/t^* - \cos 2\pi \varphi_F \sin r_D^* \hat{t}/t^* \end{aligned} \quad (39)$$

in which (28), (29) and (30) have been used. Then (35) becomes

$$G'(\hat{t}) - \frac{1}{t^*} G(\hat{t}) = \sin 2\pi \varphi_F (\cos r_D^* \hat{t}/t^* - 1) + \cos 2\pi \varphi_F \sin r_D^* \hat{t}/t^* \quad 0 \leq \hat{t} \leq \Delta t_s. \quad (40)$$

The solution to (39) subject to $G(0) = 0$, is

$$\begin{aligned} G(\hat{t}) &= t^* \left\{ c_1 r_D^* e^{\hat{t}/t^*} + \sin 2\pi \varphi_F - c_1 \sin(r_D^* \hat{t}/t^*) - c_2 \cos(r_D^* \hat{t}/t^*) \right\} \\ G'(\hat{t}) &= r_D^* \left\{ c_1 e^{\hat{t}/t^*} - c_1 \cos(r_D^* \hat{t}/t^*) + c_2 \sin(r_D^* \hat{t}/t^*) \right\} \end{aligned} \quad (41)$$

where the constants c_1 and c_2 are given by

$$c_1 = \frac{1}{D}(\cos 2\pi\varphi_F - r_D^* \sin 2\pi\varphi_F) \quad c_2 = \frac{1}{D}(r_D^* \cos 2\pi\varphi_F + \sin 2\pi\varphi_F) \quad D = 1 + (r_D^*)^2. \quad (42)$$

The separation time $\hat{t} = \Delta t_s$ is obtained from the requirement that the stress be zero. With the use of (33), (39) and (41), the stress at the failure point is written

$$\sigma|_{x=x_F} = \sigma_z \left\{ \sin 2\pi\varphi_F \cos(r_D^* \hat{t}/t^*) + \cos 2\pi\varphi_F \sin(r_D^* \hat{t}/t^*) - G' \right\}. \quad (43)$$

Therefore, Δt_s is the solution to

$$\sin 2\pi\varphi_F \cos(r_D^* \Delta t_s/t^*) + \cos 2\pi\varphi_F \sin(r_D^* \Delta t_s/t^*) - G'(\Delta t_s) = 0; \quad (44)$$

or, after some algebra,

$$c_1 r_D^* e^{\Delta t_s/t^*} - c_1 \sin(r_D^* \Delta t_s/t^*) - c_2 \cos(r_D^* \Delta t_s/t^*) = 0. \quad (45)$$

For plotting purposes, we define a parameter, η_F , that provides a measure of the propensity for failure to occur

$$\eta_F = \frac{\sigma_z - \tau_m}{\sigma_z} \quad 0 \leq \eta_F \leq 1. \quad (46)$$

With the use of (30), φ_F is related to η_F as follows

$$\sin 2\pi\varphi_F = 1 - \eta_F \quad \cos 2\pi\varphi_F = (\eta_F(2 - \eta_F))^{1/2}. \quad (47)$$

Solutions to (45) for separation time as a function of the dimensionless parameters, η_F and r_D^* , are plotted in Fig. 3. If $\eta_F = 0$, the stress is just large enough to initiate decohesion and it might be expected that the time for separation might be extremely large. On the other hand, if $\eta_F = 1$, the imposed stress is much larger than the failure initiation stress, and failure, as expected, occurs instantaneously. We note that as the duration of the pulse increases, that is for lower values of r_D^* , the time for separation increases.

In Fig. 4, we plot the stress as a function of position for a sequence of times starting with the failure initiation time. At the failure point, we see that the stress drops with time, as it ought to. However for a subdomain centered at $x = x_F$, the stress rises above the failure stress ($0.75\sigma_z$), a result of the assumption that failure occurs at only one point in the above analysis. Failure would occur everywhere in this subdomain if failure were allowed to initiate whenever the stress is above the failure stress. If the strength of the material is spatially random, then failure may initiate at a number of discrete points. This type of mechanism is consistent with specimens dissected after experiments that show a number of potential spall planes (Shockey, *et al.*, 1974; Brara, *et al.*, 2001).

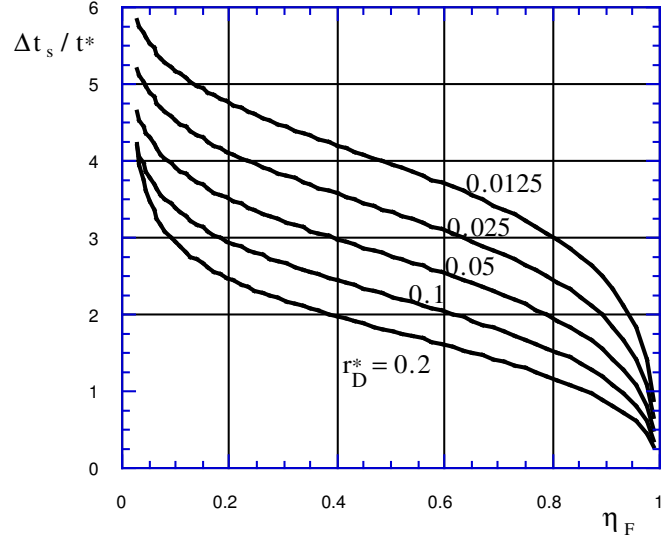


Figure 3: Dimensionless separation time, $\Delta t_s / t^*$, as a function of η_F , for various values of r_D^* .

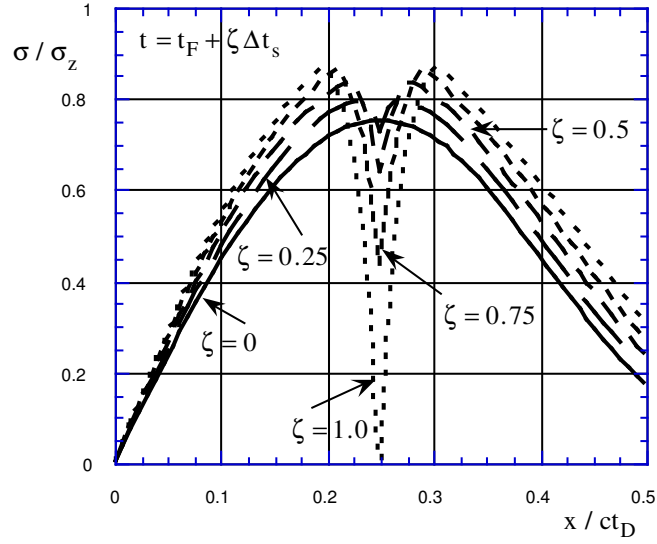


Figure 4: Dimensionless stress, σ / σ_z , as a function of dimensionless position, x / ct_D , at various times just after failure is initiated, for $\eta_F = 0.25$, $r_D^* = 0.126$, $\Delta t_s = 2.61 t^*$, and $t^* = 0.02 t_D$.

4 The Material-Point Method

The material-point method (MPM) is a general numerical technique for solving continuum mechanics problems. In this section, we review the basic method and describe how the decohesion model can be implemented in the MPM framework. In the next section, we will use MPM with the decohesion model for dynamic simulations of material failure.

Continuum mechanics models the deformation of a body described by Cauchy's equations of motion in the current configuration

$$\nabla \cdot \boldsymbol{\sigma} + \rho \mathbf{b} = \rho \mathbf{a}. \quad (48)$$

In this equation, the Cauchy stress is $\boldsymbol{\sigma}$, ρ is the mass density, \mathbf{b} is the specific body force and \mathbf{a} is the acceleration. Transformations can be made as necessary to obtain alternative stress tensors for use in constitutive equations. Similarly, the appropriate strain tensor can be developed from the deformation gradient at the end of the previous load step and the velocity gradient at the current step with the assumption that the deformation with each step is infinitesimal. We are concerned primarily with material failure of brittle materials, so large rigid body motions may occur. However, since the strains are small, and our model problems preclude large rotations, we choose to focus the presentation on the essential aspects of the numerical simulation of decohesion in the context of small deformations.

The material-point method (Sulsky *et al.*, 1994; Sulsky *et al.*, 1995; Sulsky and Schreyer, 1996) uses unconnected Lagrangian material points distributed throughout the volume of a solid body to discretize materials. The material points in the numerical solution carry properties such as mass, momentum, stress, and strain. The points move through an Eulerian spatial mesh that is used to compute the interactions between the material points. Thus, information carried by the material points is projected onto the spatial mesh, where the momentum equation is solved. This projection avoids solution techniques that involve computing pairwise interactions, so the computational work in MPM is linear in the number of material points. The material points are updated using the solution obtained on the mesh. In particular, the constitutive equation (of any type) is evaluated at the material points. Since material points are not logically connected, connectivity of the points does not have to be broken or redefined after failure.

Let \mathbf{x}_p^n , $p = 1, \dots, N_p$ denote the current position of material point p at time $t = t_n$, $n = 0, 1, \dots, N$. Each point at time t_n has an associated mass, m_p , density, ρ_p^n , velocity, \mathbf{v}_p^n , Cauchy stress tensor, $\boldsymbol{\sigma}_p^n$, strain, \mathbf{e}_p^n , and any other internal variables necessary for the constitutive model. If temperature changes are important, internal energy or temperature may also be ascribed to the material points. The material-point mass is constant in time, insuring that the continuity equation is satisfied. Other variables must be updated with reference to conservation of momentum, conservation of energy, and a constitutive equation. To make computations tractable, at each time step of a dynamic algorithm, information from the material points is interpolated to a background computational mesh. This mesh covers the computational domain and is chosen for computational convenience. A particularly simple choice is a regular rectangular grid. After information is interpolated to the grid,

equations of motion are solved on this mesh which is implemented as an updated Lagrangian frame. For example, to solve the momentum equation on the grid using an explicit FE algorithm, requires the value of the momentum at the nodal positions, at the beginning of the timestep. The nodal momentum, $m_i^n \mathbf{v}_i^n$, is the product of the nodal mass and nodal velocity, and each is determined by interpolation,

$$m_i^n = \sum_{p=1}^{N_p} m_p N_i(\mathbf{x}_p^n) \quad (49)$$

$$m_i^n \mathbf{v}_i^n = \sum_{p=1}^{N_p} m_p \mathbf{v}_p^n N_i(\mathbf{x}_p^n) \quad (50)$$

In the above, $N_i(\mathbf{x})$ is the nodal basis function associated with node i , constructed from the tensor product of piecewise linear functions. The internal forces are determined from the particle stresses according to

$$\mathbf{f}_i^{\text{int}} = - \sum_{p=1}^{N_p} \mathbf{G}_{ip}^n \sigma_p^n m_p / \rho_p^n. \quad (51)$$

The quantity \mathbf{G}_{ip}^n is the gradient of the nodal basis function evaluated at the material point position, $\mathbf{G}_{ip}^n = \nabla N_i(\mathbf{x})|_{\mathbf{x}_p^n}$. The momentum equation is solved with the nodes moving with the deformation, resulting in nodal velocities, \mathbf{v}_i^L , at the end of the Lagrangian time step of size Δt ,

$$m_i^n \frac{\mathbf{v}_i^L - \mathbf{v}_i^n}{\Delta t} = \mathbf{f}_i^{\text{int}}. \quad (52)$$

At the end of this Lagrangian step, the new nodal velocity values are used to update the material points. The material points move along with the nodes according to the solution given throughout the elements by the nodal basis functions

$$\mathbf{x}_p^{n+1} = \mathbf{x}_p^n + \Delta t \sum_{i=1}^{N_n} \mathbf{v}_i^L N_i(\mathbf{x}_p^n). \quad (53)$$

Similarly, the material point velocity is updated via

$$\mathbf{v}_p^{n+1} = \mathbf{v}_p^n + \sum_{i=1}^{N_n} (\mathbf{v}_i^L - \mathbf{v}_i^n) N_i(\mathbf{x}_p^n). \quad (54)$$

The sums in these last two equations extend from 1 to N_n where N_n is the number of nodes in the computational mesh. A strain increment for each material point is determined using the gradient of the nodal basis function,

$$\Delta \mathbf{e}_p = \frac{\Delta t}{2} \sum_{i=1}^{N_n} [\mathbf{G}_{ip}^n \mathbf{v}_i^L + (\mathbf{G}_{ip}^n \mathbf{v}_i^L)^T] \quad (55)$$

This strain increment is then used to update the stress at the material point with an appropriate constitutive equation for each material. Any internal variables necessary in the constitutive model can also be assigned to the material points and transported along with them. Once the material points have been completely updated, the computational mesh may be discarded and a new mesh can be defined, if desired; and the next timestep is begun.

The approach involving a combination of a background mesh and material points can accommodate large deformations without mesh tangling. Since the computational mesh is under user control, it can be chosen so that reasonable time steps may be taken in this Lagrangian frame. Usually, the time step is restricted by the CFL condition for an explicit algorithm, where the critical time step is the ratio of the mesh size to the wave speed. Note that this condition depends on the more favorable mesh spacing, not the material-point spacing. Since equations are solved in an updated Lagrangian frame on the FE mesh, the nonlinear convective terms troublesome in Eulerian formulations are not an issue. Finally, the material points transport material properties and internal variables without error.

In general, there is no need to determine the actual shape of the deformed material element associated with each material point. However, when material separation occurs, there is a need to consider the effect on the strain field over the element (compatibility). The increment in strain, $\Delta \mathbf{e}$, and the increment in decohesion, $\Delta \mathbf{u}^d$, are approximated by constants over each element. The failure mode is the unit vector $\mathbf{m} = \Delta \mathbf{u}^d / |\Delta \mathbf{u}^d|$. For a given time increment, if the total (average) strain increment is considered fixed, the result of the decohesion is that the effective strain increment in the remaining part of the material in the element must be reduced (relaxed) by what might be called a decohesion strain increment, $\Delta \mathbf{e}^d$, which satisfies a weak form of the compatibility condition

$$\int \Delta \mathbf{e}^d dV = \int |\Delta \mathbf{u}^d| \frac{1}{2} (\mathbf{n} \otimes \mathbf{m} + \mathbf{m} \otimes \mathbf{n}) dA, \quad (56)$$

in which dV and dA denote differentials of volume on the element and of area on the decohesion surface, respectively. With the assumption that the decohesion and strain are constant over each element, the result is the following expression relating the “relaxation” or “decohesion” strain increment to the increment in decohesion

$$\Delta \mathbf{e}^d = \frac{|\Delta \mathbf{u}^d|}{2L} (\mathbf{n} \otimes \mathbf{m} + \mathbf{m} \otimes \mathbf{n}). \quad (57)$$

The effective length, L , is merely the ratio of the element volume to the area of the decohesion surface within that element.

To summarize the implementation of the decohesive constitutive model in MPM, stress and strain are material-point properties, and the constitutive equation is evaluated for each material point in the simulation. For simplicity, assume that the basic undamaged material is elastic. The constitutive equation for elasticity is written

$$\boldsymbol{\sigma} = \mathbf{E} : \mathbf{e}^e. \quad (58)$$

The stress $\boldsymbol{\sigma}$ is related to the elastic strain \mathbf{e}^e through a fourth order elasticity tensor \mathbf{E} . The elastic strain is the difference between the total strain and the decohesion strain, $\mathbf{e}^e = \mathbf{e} - \mathbf{e}^d$.

Given the normal and tangent to the decohesion surface, \mathbf{n} and \mathbf{t} , the traction on the surface is $\boldsymbol{\tau} = \boldsymbol{\sigma} \cdot \mathbf{n}$ with normal component $\tau_n = \boldsymbol{\tau} \cdot \mathbf{n}$, and tangential component $\tau_t = \boldsymbol{\tau} \cdot \mathbf{t}$. The equations that must be solved are as follows.

1. For each loading step in the numerical procedure, compute a trial elastic stress.
2. Check the failure surface. If $F < 0$ then the step is elastic and no further calculation is required. If $F \geq 0$, failure occurs. If failure has occurred previously for the material point then the normal and tangent to the decohesion surface are known. If not, use the failure initiation criterion to determine the normal and tangent to the surface. (Note, in this work, decohesion is not allowed for negative normal tractions. Stress is positive in tension.)
3. If $F \geq 0$, the stress must be adjusted and u^{eff} incremented to restore the consistency condition $F = 0$. The stress is adjusted by evolving the opening displacement, or decohesion displacement, \mathbf{u}^d , according to

$$\dot{\mathbf{u}}^d = \dot{u}^{\text{eff}} \mathbf{m} \quad (59)$$

where the failure mode \mathbf{m} is

$$\mathbf{m} = \frac{U_0}{\tau^{\text{eff}}} \left(\frac{\tau_n}{\tau_{nf}^2} \mathbf{n} + \frac{\tau_t}{\tau_{tf}^2} \mathbf{t} \right). \quad (60)$$

A corresponding evolution for decohesion strain is defined by

$$\dot{\mathbf{e}}^d = \frac{\dot{u}^{\text{eff}}}{2L} (\mathbf{m} \otimes \mathbf{n} + \mathbf{n} \otimes \mathbf{m}), \quad (61)$$

where L is an effective length.

Iteration is required to find the solution to $F = 0$ where F is considered to be a function of u^{eff} . We use the secant method to find the zero of F .

5 Numerical Examples

The first example examines the numerical solution to the spall problem of Section 3 using a bar with uniform cross-sectional area, and uniform initial density ρ_0 . Dimensionless variables are used in the numerical simulations, where lengths are measured in units of $\mathcal{L} = ct_D$, time in units of $\mathcal{T} = t_D$ and mass in units of $\mathcal{M} = \tau_m ct_D^3$. As before, the constant c is the wave speed, $c^2 = E/\rho_0$, and t_D is the duration of the initial sinusoidal pulse. The bar has length $1.5\mathcal{L}$ units (x -direction), and is $0.5\mathcal{L}$ units high (y -direction). A prescribed velocity is input at the right end and the left end is free. Uniaxial strain conditions are imposed by constraining the lateral surfaces. With this scaling, the units of stress are $\mathcal{M}/\mathcal{T}^2\mathcal{L} = \tau_m$. The basic material is elastic with a Young's modulus, $Y = 1024\tau_m$, and Poisson's ratio,

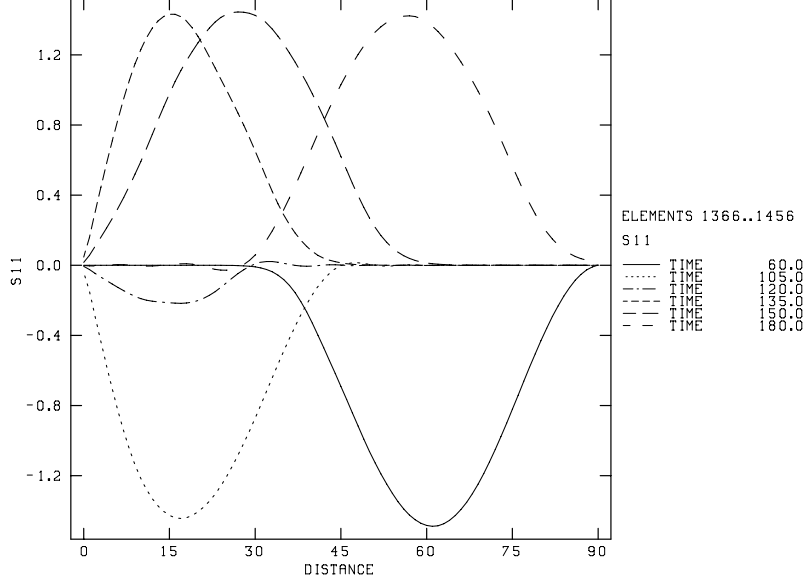


Figure 5: Dimensionless stress, σ/τ_m , *vs.* distance x along the midline in a purely elastic bar at various times due to a sinusoidal, compressive input of duration $t_D = 60$ at the right which reflects as a tensile wave from the free, left end.

$\nu = 0.25$, making the elastic modulus for uniaxial strain $E = 1228.80\tau_m$. The peak stress for the input wave is $\sigma_z = 1.5\tau_m$; and the peak velocity is then $v_z = 0.00122c$. The input pulse is in the x -direction given by $v = v_z(1 - \cos(\pi t/t_D))$, for $t \leq t_D$, where t is time and $t_D = 60$ is the duration of the pulse.

The input velocity on the right end of the bar causes a compressive pulse to travel down the bar. When the pulse reflects off the free end on the left, the bar is in tension. If the stress in the tensile reflection is large enough, failure will be initiated by decohesion. Figure 5 shows a reference calculation where decohesion is not allowed, so the bar is purely elastic. The left-going, initial wave travels at a velocity of $c = 1$ and therefore reaches the left boundary at time $t = 90$ and is completely reflected by $t = 150$, turning into a right-going tensile wave. The mesh for this calculation consists of square elements with side length $h = 1.0$, the time step is $\Delta t = 0.02$, and there are 4 material points per element. At this resolution, a small amount of numerical dispersion is apparent in Figure 5, particularly at the later time, $t = 150$, where the computed wave has moved more slowly and is not completely reflected as in the exact solution. Also, at time $t = 180$, the wave form is shifted slightly to the left from a complete reflection of the $t = 60$ pulse.

Localized Decohesion

In order to compare with the analytical solution, in the next test, we allow only the material points in one vertical strip of elements to follow the decohesion constitutive equation. These points are located near $x_F = ct_D/4 = 15$ where decohesion initiates. The parameters for

the decohesion are $\tau_{nf} = 1.0\tau_m$ and $\tau_{tf} = 10.0\tau_m$, so normal failure is much more likely. The dissipated energy is $U_0 = 0.00375\tau_m ct_D$. These properties provide the following values of the dimensionless parameters considered in Section 3 that characterize the decohesion: $\varphi_F = 0.116$, $t_F/t_D = 0.616$, $t^* = 2.30$, $r_D^* = 0.241$, and $\eta_F = 1/3$. Figure 6 is a plot of dimensionless stress σ_{11}/τ_m as a function of dimensionless position x/ct_D , for various times after failure $t = t_F + \zeta\Delta t_s$. For the given parameters, $\Delta t_s = 4.56$, and $t_F = 127$. (The failure time is measured from the start of the simulation. The failure time is 37 after the initial wave first impinges on the left end of the bar at $x = 0$.)

Figure 6 demonstrates the agreement between the numerical and analytical solutions. We observe that failure is occurring more slowly in the numerical simulation since complete separation occurs at a slightly later time. This discrepancy is due to the resolution of the simulation. Figure 7 shows a similar plot, for a computation where the mesh size has been reduced by a factor of two, $h = 0.5$. The accuracy is improved both in the shape of the wave and in the time to failure. Figure 8 compares the stress in the bar at an early, middle and late time. At $t = 60$ the left-going compressive, initial, sinusoidal pulse fully enters the domain; at $t = 135$ complete separation due to decohesion has just occurred. After decohesion, at $t = 150$, there is a right-going wave that has traveled down the bar and a left-going wave that has reflected from the free end at $x = 0$ resulting in a right-going compressive wave.

Distributed Decohesion

The previous results, and the analytical solution of Section 3, are based on the assumption that decohesion occurs only at one point along the bar. It can be seen from these solutions that after decohesion initiates, the stress adjacent to the decohesion point is still above the threshold level. This observation indicates that if all of the material in the bar were treated uniformly, decohesion would occur in a region rather than a single point. Figure 9 shows the stress σ_{11}/τ_m for the same simulation as above, except all of the material in the bar is subject to the decohesive constitutive model. The wave reflected from the free end is now clipped corresponding to a peak stress given by $\tau_{nf}/\tau_m = 1.0$. Compare Fig. 7 to see the difference in the progression of decohesion. At $t = 128$, decohesion is just beginning, the dip in the wave profile associated with the commencement of decohesion occurs at $x = ct_D/4 = 15$; however, at later times, decohesion quenches at this point. There eventually are two peaks in the decohesion to the right and left of the initial failure point. After decohesion, the right-going wave has a larger area than the left-going wave.

The velocity wave shown in Fig. 10 corresponds to the stress wave in Fig. 9. In Fig. 10(a), only a narrow band of material points is allowed to undergo decohesion, while in Fig. 10(b), the material is treated uniformly with respect to the constitutive model. In the former case a pronounced discontinuity is visible in the velocity field, while in the latter case the velocity appears to be smooth, but with a steep gradient in the decohesive region. A similar contrast appears in plots of the effective opening displacement, shown in Fig. 11. In Fig. 11(a), all of the displacement jump is concentrated at one point, $x = x_F = ct_D/4$, where the material is allowed to fail in the localized case. In Fig. 11(b), the displacement jump varies over a

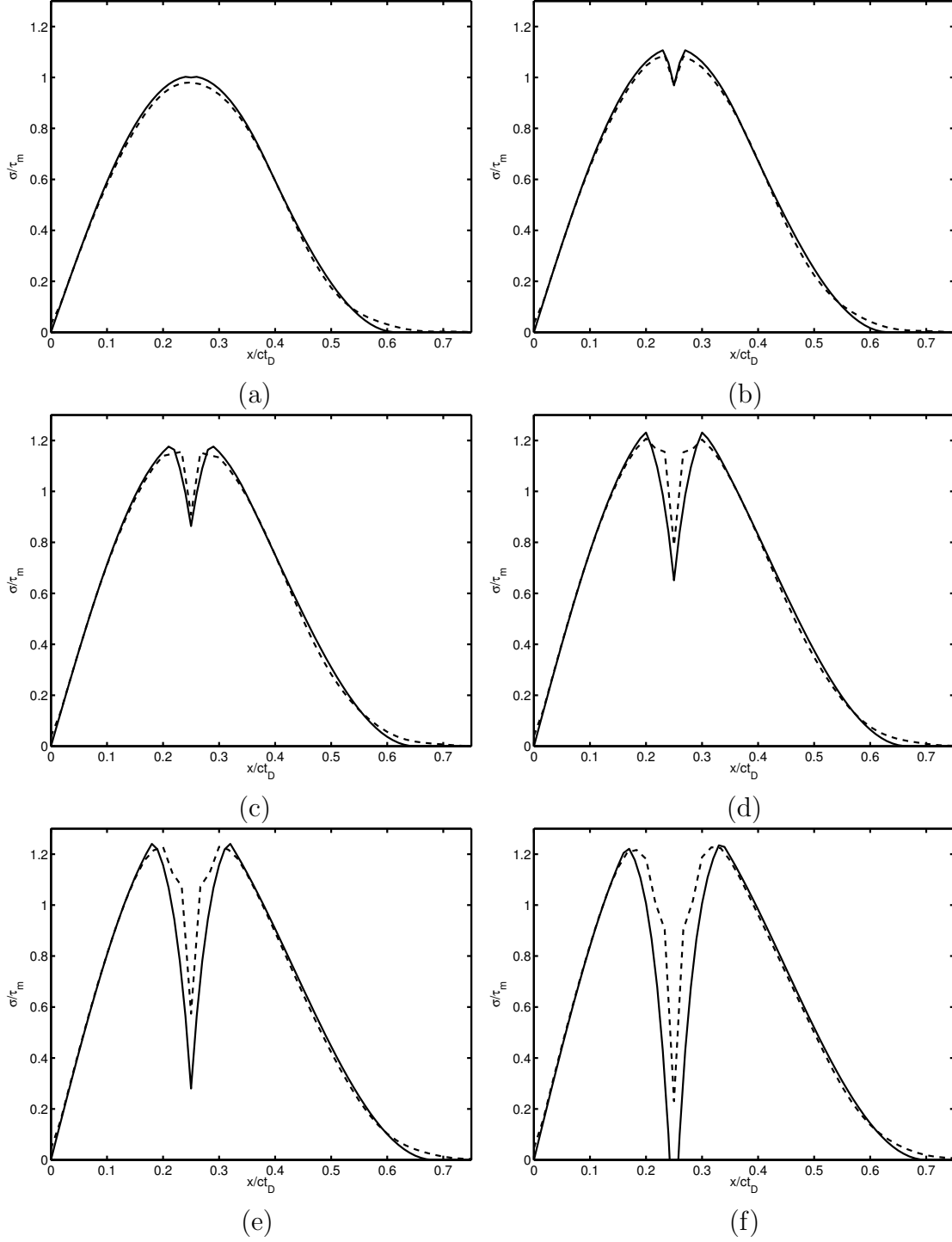


Figure 6: Plot of dimensionless stress σ_{11}/τ_m vs. dimensionless distance along the bar x/ct_D at times $t = t_F + \zeta \Delta t_s$ for (a) $\zeta = 0.0088$ ($t = 127$), (b) $\zeta = 0.2281$ ($t = 128$), (c) $\zeta = 0.4474$ ($t = 129$), (d) $\zeta = 0.6667$ ($t = 130$), (e) $\zeta = 0.8860$ ($t = 131$), (f) $\zeta = 1.1053$ ($t = 132$). The mesh size is $h = 1.0$.

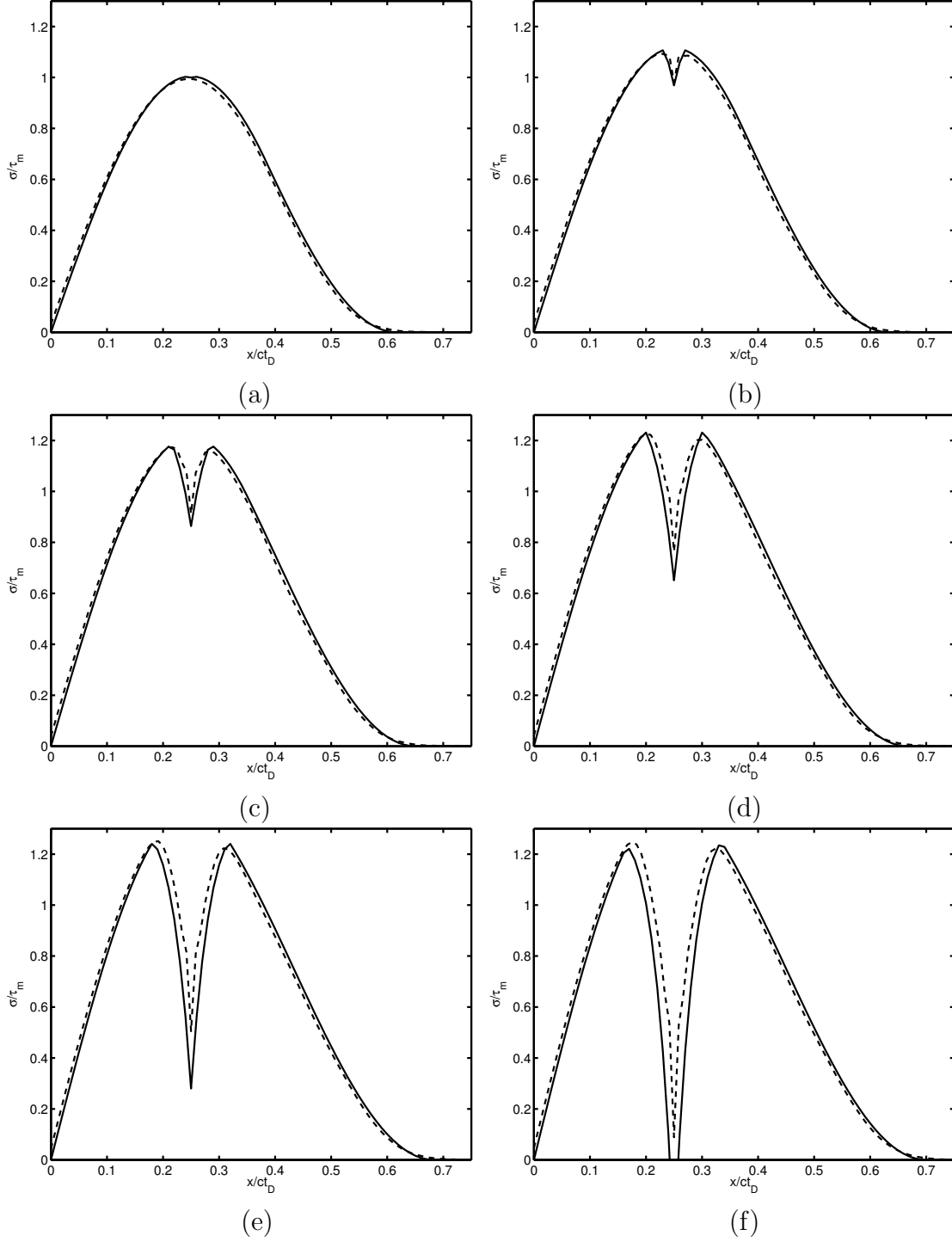


Figure 7: Plot of dimensionless stress σ_{11}/τ_m vs. dimensionless distance along the bar x/ct_D at times $t = t_F + \zeta \Delta t_s$ for (a) $\zeta = 0.0088$ ($t = 127$), (b) $\zeta = 0.2281$ ($t = 128$), (c) $\zeta = 0.4474$ ($t = 129$), (d) $\zeta = 0.6667$ ($t = 130$), (e) $\zeta = 0.8860$ ($t = 131$), (f) $\zeta = 1.1053$ ($t = 132$). The mesh size is $h = 0.5$.

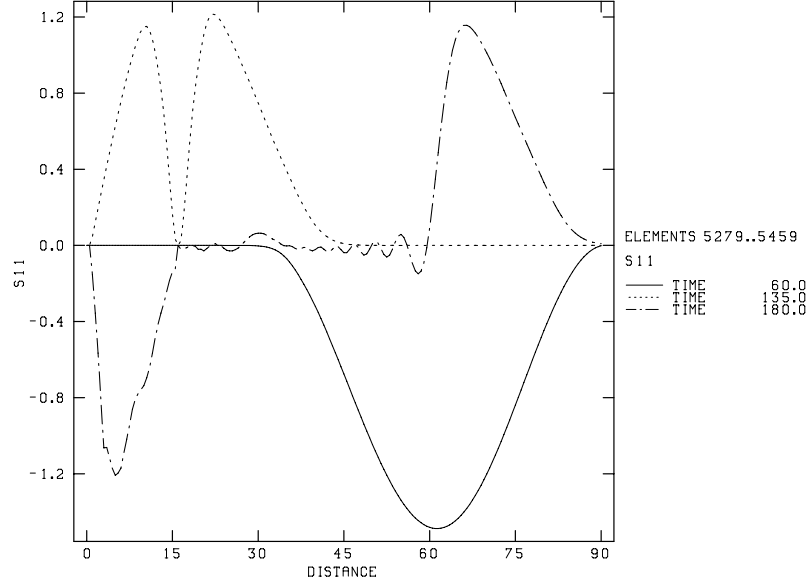


Figure 8: Stress σ_{11}/τ_m vs. distance x along the midline of a bar at $t = 60$ when the left-going compressive pulse fully enters the domain, at $t = 135$ when complete separation has occurred, and after decohesion, at $t = 150$, when the right-going wave has traveled down the bar and left-going wave has reflected from the free end at $x = 0$ resulting in a right-going compressive wave.

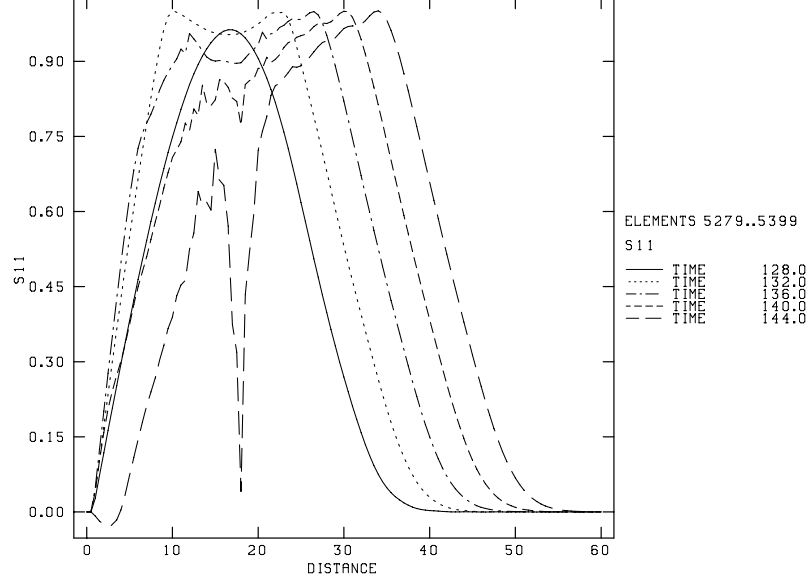


Figure 9: Stress σ_{11}/τ_m vs. distance x along the midline of a bar at $t = 128$, $t = 132$, $t = 136$, $t = 140$ and $t = 144$ showing the progression of failure in a bar with a uniformly applied decohesive model. Compare with Fig. 7 for the case where only a localized line of material undergoes decohesion.

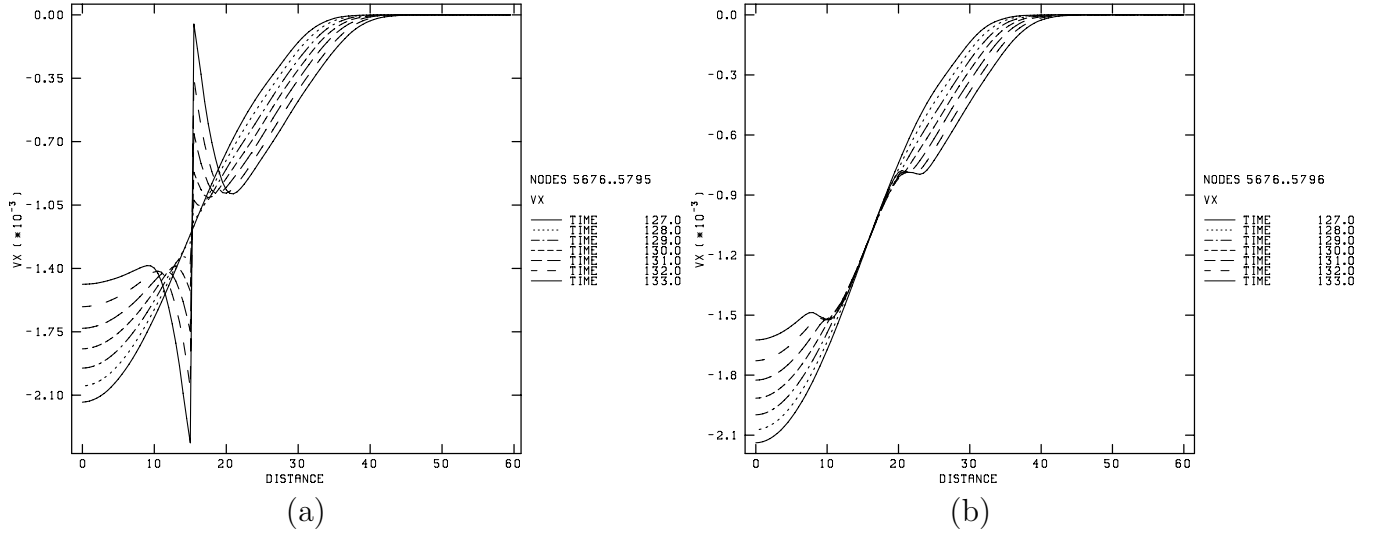


Figure 10: Horizontal component of velocity *vs.* distance along the midline of a bar at various times showing the progression of failure in a bar with (a) a localized zone of failure and (b) a uniformly applied decohesive model.

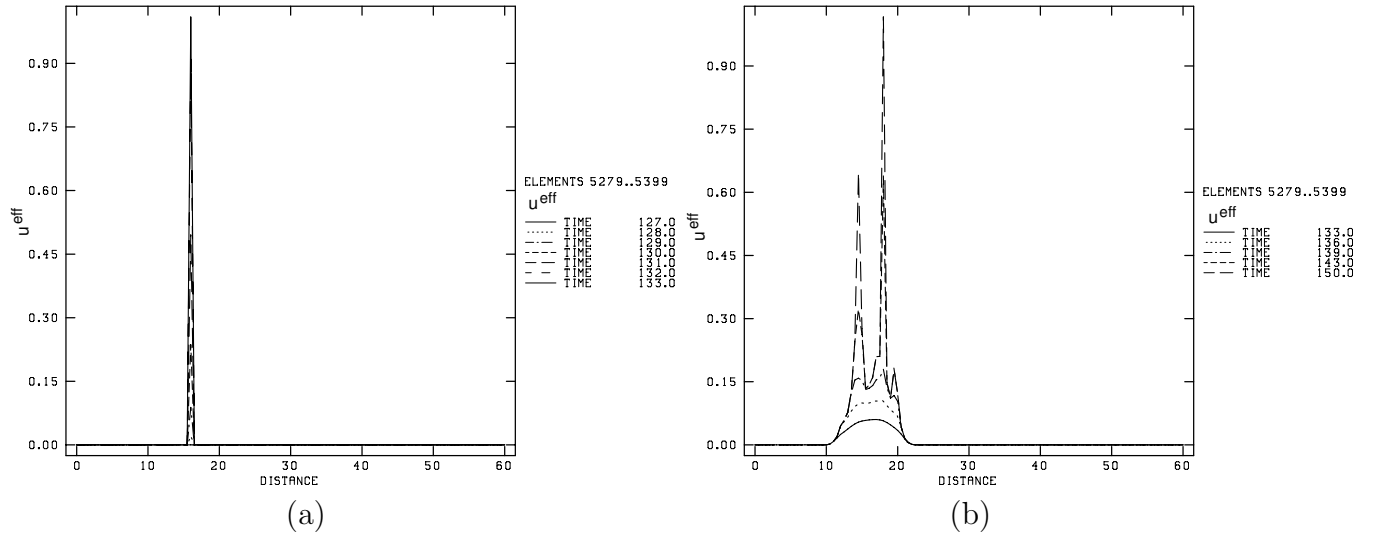


Figure 11: Effective opening displacement *vs.* distance along the midline of a bar at various times showing the progression of failure in a bar with (a) a localized zone of failure and (b) a uniformly applied decohesive model.

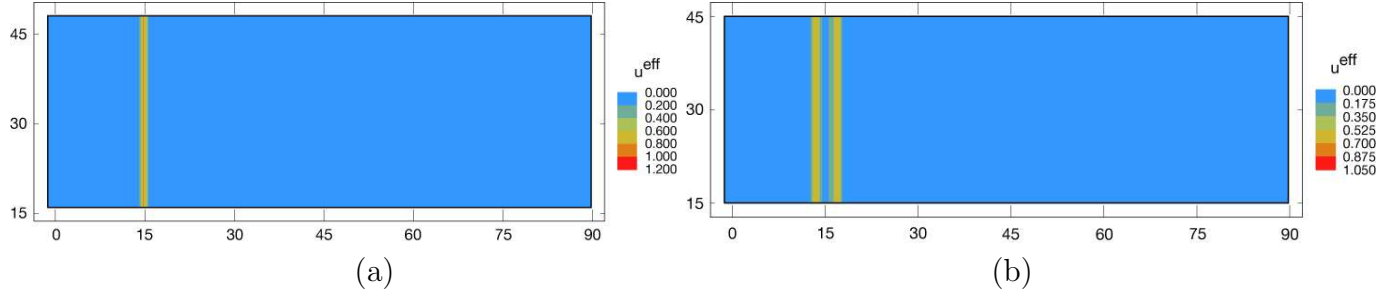


Figure 12: Contour plot of the effective opening displacement showing a zone centered around $x = 15$ where decohesion has occurred for (a) decohesion applied only in a strip and (b) decohesion applied uniformly.

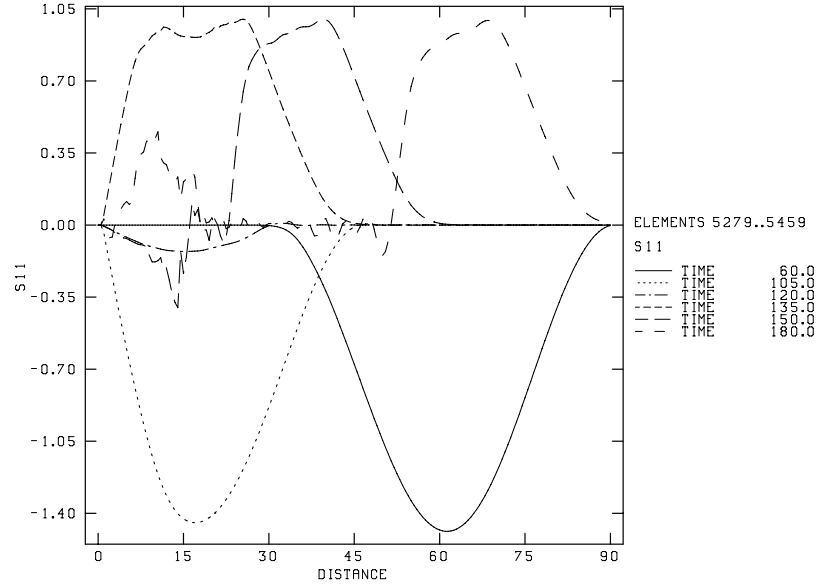


Figure 13: (a) Stress σ/τ_m vs. distance x along the midline of a bar at various times due to a sinusoidal, compressive input of duration $t_D = 60$ at the right which reflects as a tensile wave from the free, left end. The reflected wave causes decohesion to occur because the peak stress $\tau_{nf}/\tau_m = 1.0$ is exceeded. For this simulation, the decohesive constitutive model is applied uniformly in the bar; compare with Fig. 8 for the case where only a localized line of material undergoes decohesion.

region of decohesion when the decohesion model is applied uniformly. At early times, the effective opening displacement has a maximum centered at $x = x_F = ct_D/4$, but at later times decohesion quenches in the center and a peak occurs to the right and left. The peak to the right actually reaches the dimensionless value 1, indicating complete failure, while the peak to the left is only 60% open.

Figure 12 shows contour plots of the effective opening displacement, u^{eff} , a measure of the amount of decohesion. In Fig. 12a, all the decohesion occurs at the material points located in a strip of elements centered at the analytically determined spall plane, $x_F = ct_D/4 = 15$. Figure 12b is the corresponding plot when decohesion is allowed everywhere in the bar. A decohesion region is observed in this case, with the main separation occurring to the right and left of $x_F = ct_D/4 = 15$. These figures are consistent with the plots shown in Figs. 11a, b. Interestingly, on a coarser mesh, these details in the decohesion zone are not resolved and the discrete solution resembles the analytical solution.

Figure 13 shows the stress waves traveling in the bar when decohesion is allowed to occur uniformly throughout the bar. This figure is a plot of dimensionless stress σ_{11}/τ_m vs. distance x along the bar and is analogous to the elastic case, Fig. 5, and the case where the decohesive zone is limited to a thin band, Fig. 8. At the early times, $t = 60$, $t = 105$ and $t = 120$, the input compressive wave and its reflection from the free end are purely elastic. At $t = 135$ decohesion is in its early stage; Fig. 9 shows the details of the decohesion. At $t = 150$ decohesion is complete and a relatively large right-going wave and small left-going wave are apparent. Compared to the wave profiles in Fig. 8, there is a larger size difference in the wave pulses after decohesion. At time $t = 180$, the right-going wave has continued to travel down the bar, while the originally left-going wave has reflected from the free end and is now a right-going compressive wave.

Plane Stress

Material in the bar is given the same properties as considered previously, with the decohesive constitutive equation applied uniformly throughout the bar, except now plane stress is assumed. This problem becomes truly two dimensional since waves reflect from the lateral free surfaces making the wave profile different at different heights in the bar. For reference, Fig. 14 shows the elastic waves along the midline and along the lower edge of the bar. In the figure, dimensionless stress, σ_{11}/τ_m is plotted versus horizontal position, x . At early times, $t = 60$, $t = 105$ and $t = 121$, the stress is compressive. The wave form shows the effects of reflections from the lateral surfaces. Times $t = 135$, $t = 151$ and $t = 180$ show tensile waves that result from reflections from the free end at $x = 0$. At the lower edge of the bar, Fig 14b, we see a tensile peak stress located near $x = ct_D/4 = 15$ at time $t = 151$ that just reaches the failure threshold, $\tau_{nf}/\tau_m = 1$. The same pattern is observed along the top of the bar, while along the midline of the bar, Fig 14a, the tensile peak stress is larger than the failure threshold and is located near $x = ct_D/2 = 30$.

Figure 15 shows the modification to the wave profiles due to decohesion. When decohesion is allowed, small regions of damage occur along the top and bottom edges of the bar near

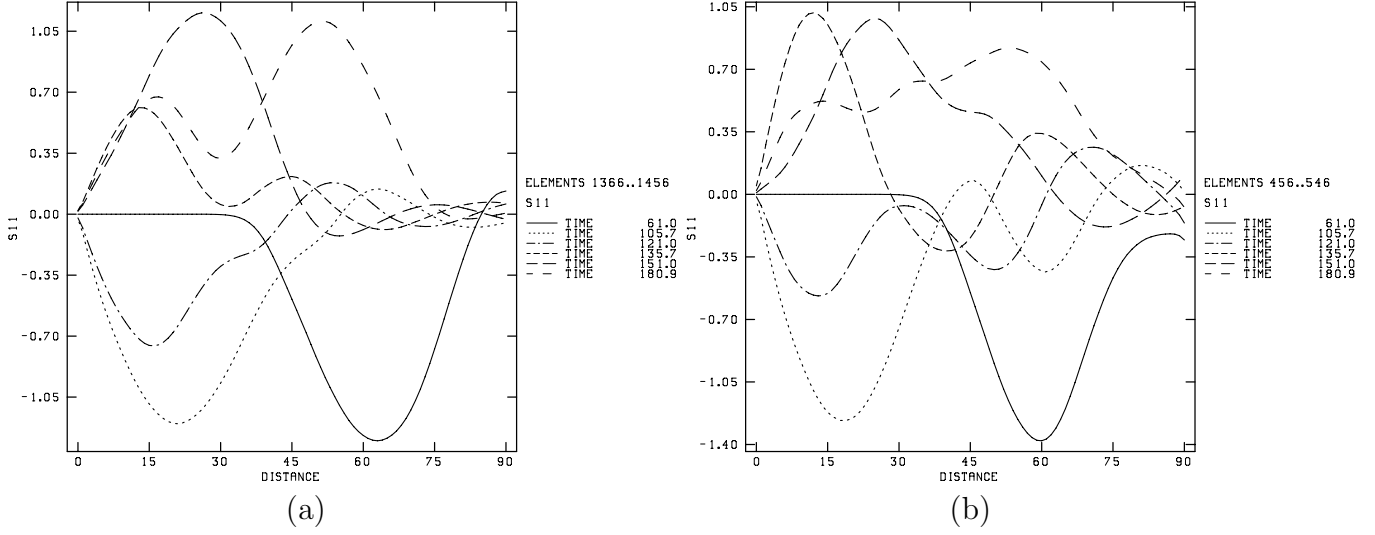


Figure 14: Dimensionless stress σ_{11}/τ_m vs. distance x at various times in a purely elastic bar under plane stress. In (a) the stress is plotted along the midline of the bar and in (b) the stress is plotted along the bottom of the bar.

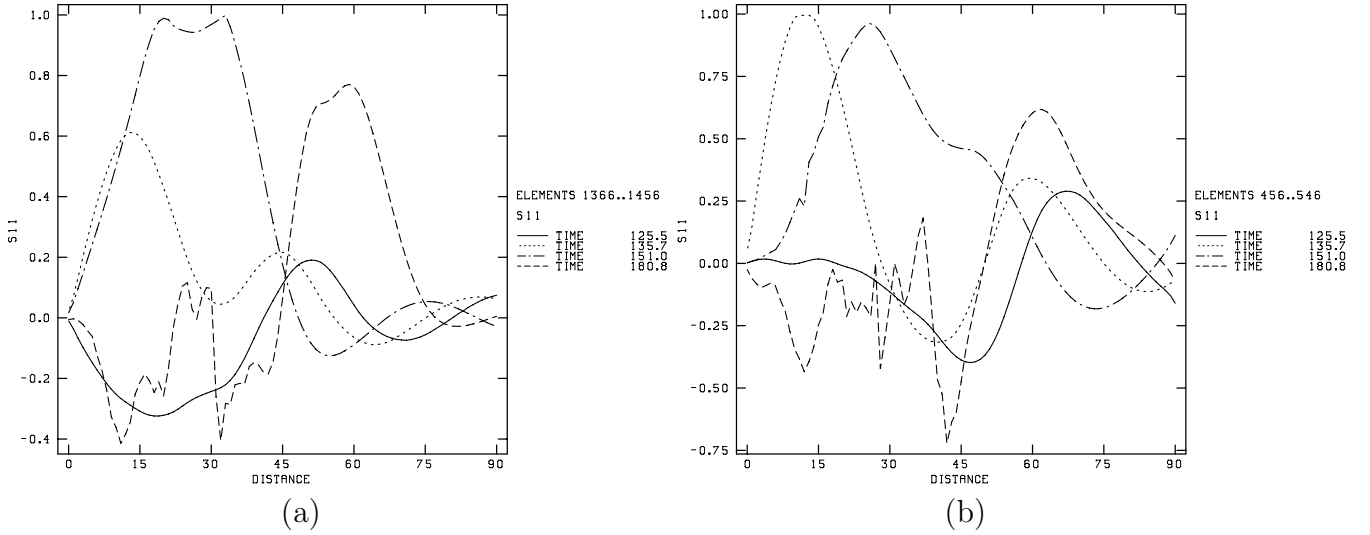


Figure 15: Dimensionless stress σ_{11}/τ_m vs. distance x at various times in a bar under plane stress with decohesion when σ_{11} reaches τ_m . In (a) the stress is plotted along the midline of the bar and in (b) the stress is plotted along the bottom of the bar.

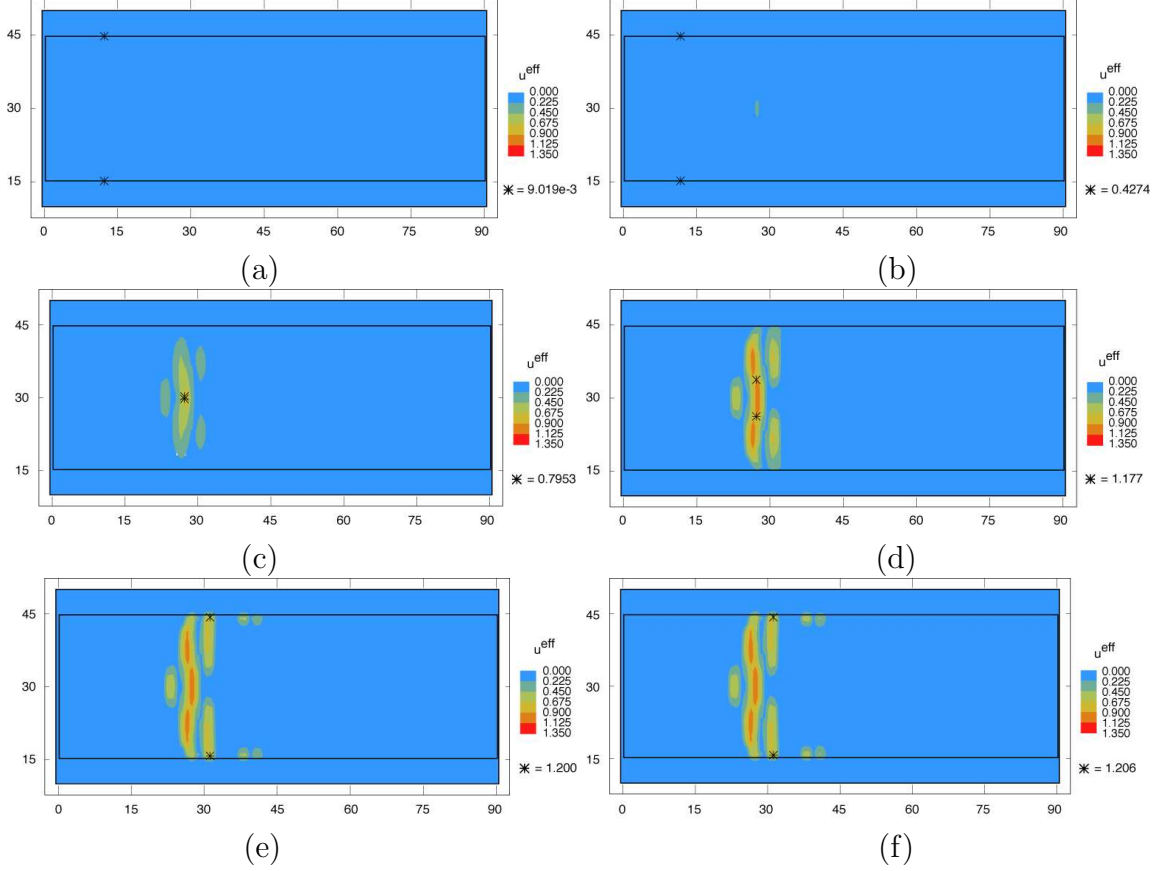


Figure 16: Contour plots of the effective opening displacement at (a) $t = 136$, (b) $t = 156$, (c) $t = 161$, (d) $t = 166$, (e) $t = 171$, (f) $t = 176$.

$x = ct_D/4 = 15$, consistent with the peak elastic stress. Note that in Fig. 15(b), the peak stress at time $t = 151$ along the lateral surface does not exceed $\tau_{nf}/\tau_m = 1$. More extensive damage occurs near $x = ct_D/2 = 30$ beginning at the midline of the bar, again consistent with the large peak stress observed in the elastic case. Figure 15(b) shows the effect of decohesion beginning at time $t = 151$ and the reduction of the right-going wave at $t = 180$. Moreover, at $t = 180$, a left-going wave initiated at the site of decohesion is apparent. Compared with Fig. 14, the peak stress does not get above $\tau_{nf}/\tau_m = 1$ throughout the bar.

Figure 16 shows the progression of failure through a sequence of contour plots of the effective opening displacement. At time $t = 136$ failure has occurred along the top and bottom lateral surfaces of the bar, as indicated by the asterisks marking the maximum effective opening displacement in Fig. 16(a). At time $t = 156$, Fig. 16(b), failure just becomes noticeable at the centerline of the bar. At later times, $t = 161$, $t = 166$, $t = 171$, the failure propagates vertically giving a damaged region located near $x = ct_D/2 = 30$ across the bar. The maximum opening displacement occurs in this region at these times. Secondary surfaces appear at $t = 161$ which also grow at later times. Additional failure appears at late stages, $t = 171$, $t = 176$, at the lateral surfaces. The interplay of waves reflecting from the

lateral surfaces in this example, conspires to form a complicated picture of failure. Two aspects of the failure process appear under plane stress that are not apparent under uniaxial strain. First, the spall surface is not flat and secondary failure regions occur away from the main spall surface. Second, the main spall region is displaced further from the free end at $x = 0$ under plane stress as compared with uniaxial strain.

6 Conclusion

A decohesive constitutive model combined with elasticity has been presented to study failure in brittle materials. The specific model belongs to a class of models introduced in Schreyer, *et al.* (2002). This paper presents a simple initiation criterion that can be used to determine the initial direction of the failure plane. The model has been implemented in the material-point method for numerical simulations.

The response of a bar to an applied, sinusoidal, stress pulse has been examined both analytically and numerically. In the analytical solution, a restriction to uniaxial stress or strain is made; and it is also assumed that decohesion can occur at one point only. These assumptions reduce the problem to one dimension and make the analysis tractable. The solution is given for the initial stages of decohesion, up to the point where the bar separates into two pieces. Numerical simulations using uniaxial strain, and allowing failure to occur only at the analytically determined location, faithfully reproduce the details of the analytical failure pattern.

The numerical simulations are extended to allow all of the material in the bar to be subjected to failure as governed by the decohesive constitutive model. As expected, failure occurs in a region of the bar rather than at a single point. The major damage is displaced slightly from the location obtained under the assumptions of the analytical solution. The resulting wave pattern is altered so that there is less symmetry between the two sides of the spall plane. Additional simulations relax the uniaxial strain assumption to plane stress. The resulting problem is truly two dimensional. The complex interaction of waves produces a progression of damage that starts near the lateral surface of the bar, and eventually includes a spall surface that initiates from damage along the midline of the bar. The spall surface is located further from the free end of the bar as compared with the one-dimensional examples.

The decohesion constitutive model is a conceptually simple means to model material failure. Prior to failure, decohesion can be combined with elasticity or other constitutive models to account for brittle behavior or varying amounts of ductility. The formulation is thermodynamically consistent and correctly accounts for dissipated energy. In contrast to softening plasticity, the underlying equations remain well-posed and the stress carrying capacity of the material is diminished anisotropically in accordance with the traction-displacement relation enforced on the failure surface. Numerical simulations demonstrate the dynamic determination of the initiation and direction of failure using the decohesive model. In combination with MPM, a flexible tool has been developed for the analysis of dynamic failure. In particular, MPM enforces constitutive equations at material points; when decohesion occurs at these points there is no need to duplicate nodes or otherwise remesh. Separation of surfaces

is allowed as part of the numerical solution since connections between material points are not explicit, but exist only through interactions of material points with field variables on the background mesh.

Acknowledgments:

This material is based upon work supported by the National Science Foundation under Grant Nos. DMS0074325 and DMS9102975.

References

- [1] F. Armero, 1999, Large-scale modeling of localized dissipative mechanisms in a local continuum: applications to the numerical simulation of strain localization in rate-dependent inelastic solids, *Mechanics of Cohesive-Frictional Materials* 4, 101-131.
- [2] F. Armero, 2002, On the Characterization of Localized Solutions in Inelastic Solids: An Analysis of Wave Propagation in a Softening Bar, *Comput. Meths. Appl. Mech. Engrg.*, 191, 181-214.
- [3] F. Armero, and K. Garikipati, 1996, An analysis of strong discontinuities in multiplicative finite strain plasticity and their relation with the numerical simulation of strain localization in solids, *Int. J. of Solids and Structures*, 33(3-5), 2863-2885.
- [4] G. I. Barenblatt, 1959, The formation of equilibrium cracks during brittle fracture; general ideas and hypotheses: axially symmetric cracks, *J. Appl. Math. Mech.*, 23, 622-636.
- [5] A. Brara, F. Camborde, J. R. Klepaczko, and C. Mariotti, 2001, Experimental and numerical study of concrete at high strain rates in tension, *Mechanics of Materials*, 33, 33-45.
- [6] G. T. Camacho and M. Ortiz, 1996, Computational Modelling of Impact Damage in Brittle Materials, *Int. J. of Solids and Structures*, 33(20-22), 2899-2938.
- [7] R. Clos, U. Schreppel, U. Zencker, T. Rahmel, K. Klenk, and U. Mayer, 1991, Crack propagation and arrest study at stress pulse loading. In "Dynamic failure of materials," H.P. Rossmannith and A.J. Rosakis, Eds., Elsevier Applied Science, New York, 1991.
- [8] A. Corigliano, 1993, "Formulation, identification and use of interface models in the numerical analysis of composite delamination," *Int. J. Solids Structures*, 30(20), 2779-2811.
- [9] E. Dvorkin, A.M. Cuitino, and G. Gioai, 1990, Finite Elements with Displacement Interpolated Embedded Localization Lines Insensitive to Mesh Size and Distortions, *Int. J. for Num. Methods in Eng.*, 30, 541-564.

- [10] D.E. Grady and M.E. Kipp, 1979, The micromechanics of impact fracture of rock, *Int. J. Rock Mech. Min. Sci. & Geomech. Abst.*, 16, 293-302.
- [11] P.H. Feenstra, R. de Borst, and J.G. Rots, 1991a, Numerical Study of Crack Dilatancy. I: Models and Stability Analysis, *J. of Engineering Mechanics*, 117, 733-753.
- [12] P. H. Feenstra, R. de Borst, and J.G. Rots, 1991b, Numerical Study of Crack Dilatancy. II: Applications, *J. of Engineering Mechanics*, 117, 754-769.
- [13] A. Hillerborg, M. Modeer, and P.-E. Petersson, 1976, Analysis of Crack Formation and Crack Growth in Concrete by Means of Fracture Mechanics and Finite Elements, *Cement and Concrete Research*, 6, 773-782.
- [14] G. R. Johnson and T. J. Holmquist, 1992, A computational constitutive model for brittle materials subjected to large strains, high strain rates, and high pressures, In "Shock-Wave and High-Strain Rate Phenomena in Materials," E.A. Meyers, L.E. Murr and K.P. Staudhammer, Eds., Marcel Dekker, New York, pp. 1075-1081.
- [15] R. Larsson and K. Runesson, 1996, Element-embedded localization band based on regularized displacement discontinuity, *J. of Engineering Mechanics*, 122(5), 402-411.
- [16] C. Miehe and J. Schröder, 1994, Post-critical discontinuous localization analysis of small-strain softening elastoplastic solids, *Archive of Applied Mechanics*, 64, 267-285.
- [17] A. Needleman, 1987, A continuum model for void nucleation by inclusion debonding, *J. of Applied Mechanics*, 54, 525-531.
- [18] J. Oliver, 1996a, Modelling strong discontinuities in solid mechanics via strain softening constitutive equations. Part 1: Fundamentals, *Int. J. for Num. Methods in Eng.*, 39, 3575-3600.
- [19] J. Oliver, 1996b, Modelling strong discontinuities in solid mechanics via strain Softening constitutive equations. Part 2: Numerical simulations, *Int. J. for Num. Methods in Eng.*, 39, 3601-3623.
- [20] J. Oliver, 2000, On the discrete constitutive models induced by strong discontinuity kinematics and continuum constitutive equations, *Int. J. of Solids and Structures*, 37(48-50), 7207-7230.
- [21] M. Ortiz and A. Pandolfi, 1999, A class of cohesive elements for the simulation of three-dimensional crack propagation, *Int. J. Num. Meth. in Eng.*, 44, 1267-1282.
- [22] A. Pandolfi, P.R. Guduru, M. Ortiz and A.J. Rosakis, 2000, Three dimensional cohesive-element analysis and experiments of dynamic fracture in C300 steel, *Int. J. of Solids and Structures*, 37, 3733-3760.

- [23] J. Planas, M. Elices and G.V. Guinea, 1995, The extended cohesive crack, In “Fracture of Brittle Disordered Materials: Concrete, Rock and Ceramics,” Edited by G. Baker and B.L. Karihaloo, E&FN Spon, London, 51-65.
- [24] A.M. Rajendran, 1994, Modeling the impact behaviour of AD85 ceramic under multi-axial loading, *Int. J. Impact Engng.*, 15, 749-768.
- [25] E.D. Reedy, Jr., F.J. Mello and T.R. Guess, 1997, Modelling the initiation and growth of delaminations in composite structures, *J. of Composite Structures*, 31, 812-831.
- [26] H.L. Schreyer, D.L. Sulsky and S.-J. Zhou, 2002, Modeling delamination as a strong discontinuity with the material point method, *Comput. Meths. Appl. Mech. Engrg.*, 191, 2483-2507.
- [27] L. Seaman, D.R. Curran, and W.J. Murri, 1985, A Continuum Model for dynamic tensile microfracture and fragmentation, *J. Appl. Mech.*, 52, 593-600.
- [28] D.A. Shockey, D.R. Curran, L. Seaman, J.T. Rosenberg and C.F. Petersen, 1974, Fragmentation of rock under dynamic loads, *Int. J. Rock Mechs. Sci & Geomech. Abstr.*, 11, 303-317.
- [29] J.C. Simo, J. Oliver and F. Armero, 1993, An analysis of strong discontinuities induced by strain-softening in rate-independent solids, *Computational Mech.*, 12, 277-296.
- [30] J.C. Simo, and J. Oliver, 1994, A new approach to the analysis and simulation of strain-softening in solids, *Fracture and Damage in quasi-Brittle Materials*, ed. by Z.P. Bazant et al., Workshop held in Prague.
- [31] D. Sulsky, Z. Chen and H.L. Schreyer, 1994, A particle method for history-dependent materials, *Computer Methods in Applied Mechs. and Engineering*, 118, 179-196.
- [32] D. Sulsky, S.-J. Zhou and H.L. Schreyer, 1995, Application of a particle-in-cell method to solid mechanics, *Comput. Phys. Commun.*, 87(1&2), 236-252.
- [33] D. Sulsky and H.L. Schreyer, 1996, Axisymmetric Form of the Material Point Method with Applications to Upsetting and Taylor Impact Problems, *Comput. Meths. in Appl. Mechs. Engrg.*, 139(1-4), 409-429.
- [34] J. Walter, (Ed.), 1992, Material modeling for terminal ballistic simulation, Technical Report BRL-TR-3392, US Army Ballistic Research Laboratory, Maryland.
- [35] G.N. Wells and L.J. Sluys, 2000a, Application of embedded discontinuities for softening solids, *Engineering Fracture Mechanics*, 65, 263-281.
- [36] G.N. Wells and L.J. Sluys, 2000b, Three-dimensional embedded discontinuity model for brittle fracture, *Int. J. Solids Structures*, 38(5), 897-913
- [37] J.A. Zukas, *Impact Dynamics*, Wiley, New York, 1982.